




# The Synergy Between Corrosion and Fatigue: Failure Analysis of an Aerator and a Cooling Tower

Luciano da Rocha Magalhães · Rodrigo Freitas da Silva Alvarenga · Flávio Augusto Coelho Resende · Leonardo Rosa Ribeiro da Silva  · Waldek Wladimir Bose Filho · Sinésio Domingues Franco

Submitted: 7 July 2023 / Accepted: 7 July 2023 / Published online: 19 August 2023  
© ASM International 2023

**Abstract** Corroded points can act as stress concentrators, usually resulting in the component failure at fewer cycles than was initially projected. Aerators are widely used in waste treatment units for chemical and biological control. Due to the chemically aggressive environment to which these components are subjected, they usually fail due to corrosion in one or more components. Cooling towers are one of the most applied equipment for temperature control in industrial processes. Due to generally hostile environments and operating conditions, this equipment is subject to failures which almost always lead to system imbalance followed by the catastrophic failure of the component. This work investigates the synergic effect of corrosion and fatigue in two separate case studies. In the first, the wear of the mixing shaft of an aerator was investigated. It was observed that the root cause of wear was the corrosion of the dissimilar welded joints in the mixing blades, which suffered the sensitization phenomenon. This sensitization led to the formation of accentuated corrosion pits, which concentrated stresses and led to the failure of the welded joint. After the joint failure, the component was left in an unbalanced state, which resulted in severe wear on the mixer shaft of the aerator. In the second, the failure of a cooling tower fan shaft fracture was evaluated, with the fractured component being compared to an intact one. As means of analysis were employed: metallographic tests on

macroscopic and microscopic scales, tensile, chemical composition, hardness tests, and fractography. The results indicated the component failure due to fatigue under low amplitude loading, with corrosion pits as stress intensifiers.

**Keywords** Aerator · Cooling tower · Dissimilar weld · Fractography · Sensitization · Corrosion

## Introduction

One of the main challenges in failure analysis lies in the fact that a component failure does not always have its root cause in the region that has suffered the most damage. This is even more evident in rotating machinery components, as even a small failure leads to an imbalance of the system, which, in turn, often leads to catastrophic failure of the component as a whole [1]. Corrosion control is often stated as one of the main challenges to rotatory components, as it severely decreases component life, leading to imbalances and failure [2].

Despite corrosion and fatigue interaction being relatively well-known phenomena, identifying the same as the root cause of a failure is not easy. In general, this happens because of the small scale of the corrosion pits (that act as stress concentration points) in relation to the fractured area. Ebara [3] studied the interaction between corrosion pits and hydrogen embrittlement as crack initiators in the failure analysis of a 12 Cr stainless steel cargo oil ship steam turbine blade. The authors illustrated that the corrosion pits lead to intergranular failure, especially with the additional influence of hydrogen that enters the plastic deformation zone due to the reaction between the steel,  $H_2S$  (originated from the crude oil), and  $H_2O$ . Adedipe et al. [4] reviewed

---

L. da Rocha Magalhães · R. F. da Silva Alvarenga ·  
L. R. R. da Silva (✉) · W. W. B. Filho · S. D. Franco  
Federal University of Uberlândia, Av. João Naves de Ávila,  
2121, Uberlândia, MG 38400-902, Brazil  
e-mail: leorrs@ufu.br

F. A. C. Resende  
Mosaic Fertilizantes P&K Ltda, Fazenda Chapadão, S/N, Zona  
Rural, Catalão, GO 75701970, Brazil

the corrosion fatigue phenomena in the wind sector offshore structures. Among the variables reviewed, the authors reported the influence of load frequency, stress magnitude, cathodic protection, seawater environment, steel composition and welding characteristics. According to the authors, despite each reviewed variable having a significant influence on the corrosion, the synergy effect between those variables can significantly increase the crack propagation and thus need to be the subject of more studies.

The welding of dissimilar joints is widely used in the industry as it allows the joining of materials with different properties, thus optimizing the component in terms of attributes such as weight, mechanical, tribological, and chemical resistance [5]. According to Corleto et al. [6], these advantages resulting from the combination of different properties can result in problems, especially in operating conditions involving high temperatures or corrosive environments, where the difference in properties can result in increased distortion or corrosion of the component.

As Yin et al. [4] reported, one of the biggest problems in dissimilar welds is sensitization, which can be seen in intergranular corrosion. Alizadeh-Sh et al. [7] evaluated the microstructural evolution as a failure mode of dissimilar austenitic/duplex stainless steel welding. The authors reported that the sensitization was caused by pre-existing TiC particles on the base metal that were dissolved in the heat-affected zone, increasing the carbon concentration, and leading to sensitization, mainly in the form of intergranular corrosion. Moteshakker et al. [6] reported similar effects regarding carbide dissolution on the welding process of austenitic and duplex stainless steels. Verma et al. [8] further state that this phenomenon is further increased when the dissimilar welded joint is subjected to aggressive environments.

As stated by Udoye et al. [9], cooling towers are widely employed as one of the main structures to dissipate heat to the atmosphere in chemical and petrochemical industries as well as thermal and nuclear power plants. The fan provides an airflow that enables faster cooling of the coolant stream (usually water). Failures in this component can be critical since even with partial failures, the system will be unstable, and thus the vibration will increase, resulting in more accelerated failure.

According to Padasale et al. [10], one of the main root causes of failure in cooling towers is crack initiation due to corrosion, especially in the presence of localized corrosion pits that act as stress concentration points lowering the component fatigue life. The authors further state that failures can occur due to design flaws, wrong material choice or heat treatment, and improper manufacturing that is mainly related to the welding process, such as wrong pre-heating temperatures. In the paper, the authors evaluated

the failure of the cooling fan tower shaft and found that the root cause was localized galvanic corrosion caused by improper welding of the mild steel used in the component.

Kazempour-Liacy et al. [11] conducted a fatigue failure analysis of a forced draft fan blade made of 2014-T6 aluminum alloy. The techniques employed by the authors were visual inspection, microstructure characterization, fractography, and hardness testing. The authors reported that the fracture was caused by a crack induced by stress concentration points in pit corrosion spots caused by Cl ions.

Hegde et al. [12] evaluated the catastrophic failure of a fan employed at a urea prill tower made of Al-Si alloy. The fan was operational for 20 years and presented a sudden catastrophic failure of all blades resulting in considerable risks to the operation safety. The authors reported that the root cause was a thin denting at the blade edge, which increased due to fatigue-corrosion over the 20 years of the component workspan, leading to the blade failure, followed by the system unbalancing and failure of the other blades.

Medrea et al. [13] conducted a failure analysis of a cooling tower fan blade U-shaped DIN 1.7225 steel support assembly employed at an electrical power plant. The authors reported the component failure due to low cycle fatigue as the cracks initiated at different points and ended as a narrow detachment area. According to the authors, the root cause of the failure was improper material selection and component design.

In the present work, two failure case studies were presented. The first case study evaluating the failure of an aerator/mixer was analyzed to identify the causes of the severe wear presented by the mixer shaft and the corrosion observed in the float fastening belt. To this end, macro and micrographic investigations, hardness measurements, and chemical composition analyses were carried out on various aerator components. The second case study evaluated two cooling tower fan shafts, one fractured and the other intact, to determine the probable causes of failure. Metallographic tests (macro and micro), chemical composition analysis, hardness measurement, tensile tests, and fractography of the fracture surface were used.

## Component and Methods

### Aerator/Mixer

#### *Evaluated Component*

An OXYTARGET WTA-20 Aerator/Mixer from the manufacturer WTECH Group was analyzed to identify the causes of the severe wear presented by the mixer shaft and the corrosion observed in the float fastening strap.

This equipment is used in a process waste pond in the treatment of effluents (Fig. 1), where it has two main actions: supplying oxygen to the liquid medium and/or promoting the movement of the medium, causing the solids present to remain in suspension. According to the Contracting Party, these lakes have a high concentration of chlorides, as attested by the Chemical Report in ANNEX 1 of this report. Figure 2 illustrates an aerator/mixer of the same model as the equipment sent for analysis, highlighting the elements that showed more significant degradation. Figures 3, 4, and 5 illustrate the analyzed components.

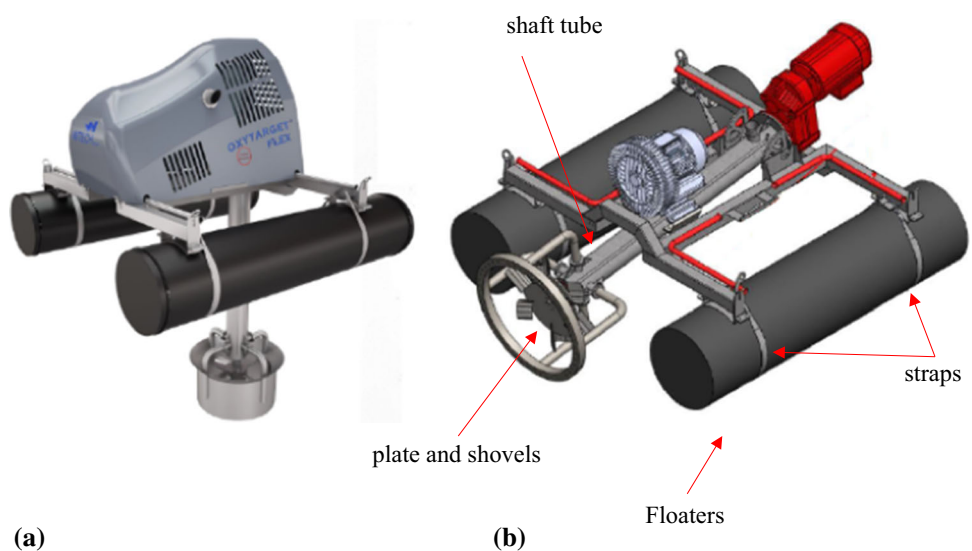
*Experimental Procedures*

After receiving the parts, the shaft, belt, plate, and blade samples were taken for chemical composition analysis and



**Fig. 1** Effluent treatment pond where aerators/mixers are used

**Fig. 2** Illustration of an aerator similar to the one analyzed (taken from the manufacturer’s manual), with (a) a photo of the equipment and (b) a CAD showing the main components



macro and microscopic investigation of wear. A part of the tip was removed from the shaft for analysis, as shown in Fig. 6, in the region of the most significant diameter loss (area highlighted in Fig. 5). Figure 7 illustrates the sampling points of the plate/blade assembly.

The metallographic preparation of the samples was performed according to the American Society for Testing and Materials (ASTM) standard E3-11 [14]. After performing the cuts, the samples were cleaned in an ultrasonic bath with ethyl alcohol. Subsequently, the samples were sanded from 120 to 1200 mesh with water sandpaper. Polishing was performed with 6, 3, and 1 μm diamond pastes, and the microstructure was revealed using Aqua Regia reagent, according to ASTM E407-07 [15] guidelines.

Macrographic analyzes were performed using a stereomicroscope from the manufacturer Optacam OPZTS equipped with the LOPT14003 14 MP camera. The microstructure, in turn, was evaluated using an Olympus optical microscope (OM), model BX51M, equipped with a Zeiss digital camera, model AxioCam ICc5 and ZenCore® software. Scanning electron microscopy was performed using a Field Emission Gun microscope, Carl Zeiss, model Supra 40.

The hardness was measured using a Stiefelmayer-Reicherter durometer, model KL-4. Vickers indentations were performed with a load of 1 kgf and application time of 30 s, according to the determinations of the ASTM E92 [16] standard. When necessary for comparison purposes, Vickers hardness values were converted to the HRC scale using ASTM E140-12B [17] determinations.

An optical emission spectrometer by glow discharge (GDS) of the brand LECO, model GDS 500, was used for the chemical composition analysis.

## Cooling Tower Fan Blade

### *Evaluated component*

Two shafts of a cooling tower fan (used in the production process of mineral fertilizers) were evaluated in order to point out the probable causes of their fracture. Figure 8, taken from the manufacturer's manual, illustrates the component overview. Figure 9, in turn, shows field photos taken after the stem breaks.

The components sent by the company for analysis are shown in Fig. 10. The fractured rod (center) was sent along with its support (left). The intact shaft (that is, one that did not fracture or present any crack) was sent without support.

In this failure analysis, the following were evaluated: (i) the fracture surface, (ii) the microstructures of the fractured and intact components, (iii) the hardness along with the



**Fig. 3** Overview of the aerator submitted for analysis

**Fig. 4** Mixer plate highlighting the blades that were already broken and the advanced corrosion in the welded joint



broken blades

thickness of both parts; (iv) the chemical composition, and (v) the tensile strength of specimens removed from the shaft (Fig. 11).

### *Experimental Procedures*

The two parts of the fractured shaft were washed with soap and water to remove residues and any other substance that could contaminate the region of interest. Next, the fracture surfaces were dried and protected from corrosion using petroleum jelly. Figure 4 shows the fracture surface of the nail after cleaning. Intense oxidation of the fracture surfaces and sides is observed.

Samples were taken from the locations as shown in Fig. 12, with an indication of the analyzes that were carried out on each sample. These cuts were performed using a refrigerated abrasive disk, in such a way as to preserve the original microstructure.

The metallographic preparation of the samples was performed according to the American Society for Testing and Materials—ASTM E3-11 [14]. After performing the cuts, the samples were cleaned in an ultrasonic bath with ethyl alcohol. Macrography of the fracture surface was performed without any preparation. The samples for micrographic analysis were sanded with water sandpaper



**Fig. 5** The fracture surface analyzed with an emphasis on the sample withdrawal region



from 120 to 1200 mesh. Polishing was performed with 6, 3, and 1-micron diamond pastes, and the microstructure was revealed using 2% Nital etchant.

The fracture surface was investigated using a stereomicroscope from the manufacturer Opticam OPZTS equipped with the LOPT14003 14 MP camera. The microstructure was evaluated using an Olympus optical microscope (OM), model BX51M, equipped with a Zeiss digital camera, model AxioCam ICc5 and ZenCore® software. Samples in the longitudinal section of the non-fractured nail, taken from the same fracture region of the fractured nail, were analyzed by scanning electron microscopy (SEM) using a Field Emission Gun microscope, Carl Zeiss, model Supra 40.

The hardness was measured using a Stiefelmayer-Reicherter durometer, model KL-4. Vickers indentations were performed with a load of 1.0 kgf and an application time of 30 seconds, according to the ASTM E92 [16] standard. An optical emission spectrometer by glow

discharge (GDS) of the brand LECO, model GDS 500, was used for the chemical composition analysis.

The tensile tests were performed according to the methodology of ASTM E8/E8M [18] using a universal testing machine, brand Instron, model 8801, consisting of a double-acting hydraulic servo actuator with a force capacity of up to ± 100 kN. The miniaturized specimens (Fig. 13) were machined by conventional machining from a central point of the shank, from the middle of the thickness

**Results and Discussions**

*Aerator/Mixer*

*Chemical Composition*

The chemical compositions of the four components can be seen in Table 1. Table 2, in turn, presents standardized



**Fig. 6** The shaft end was removed for chemical composition, hardness, and wear analysis

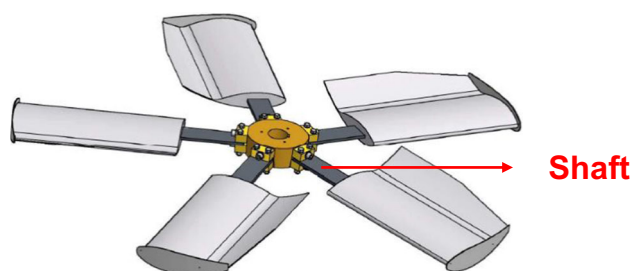


**Fig. 8** Schematic representation of the fan blades, highlighting the shaft

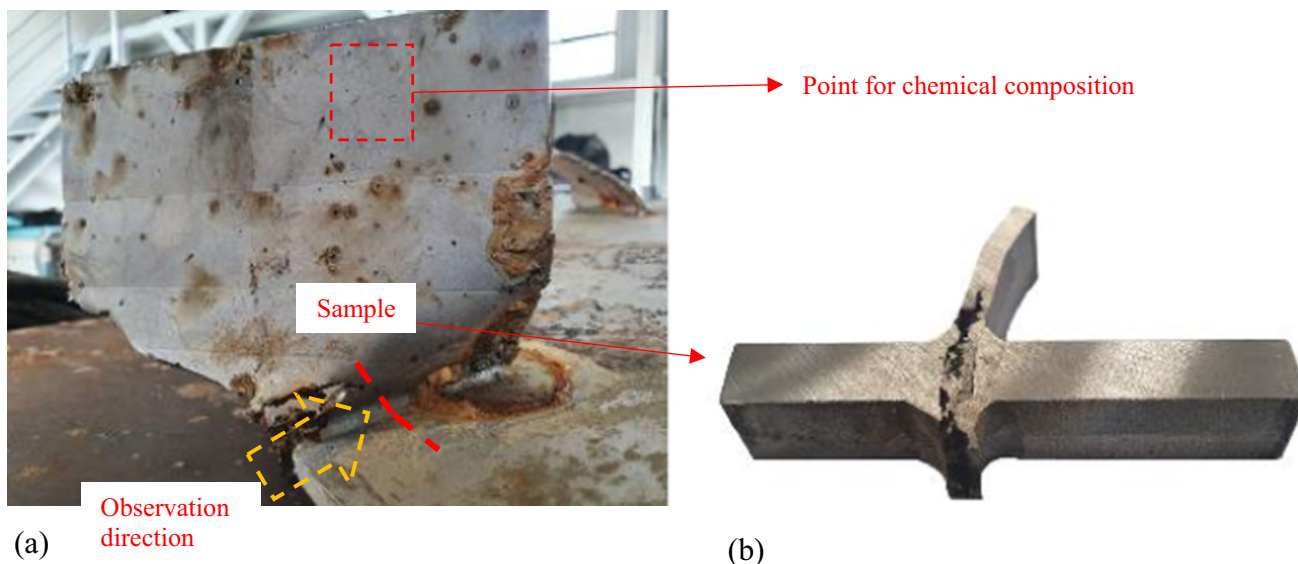


**Fig. 7** Sampling points from the plate/blade assembly, where (a) shows the blade still attached to the plate and (b) is the cross section of the weld bead for corrosion analysis

**Fig. 9** Photographs of assembled propellers (left) and fractured components (right)

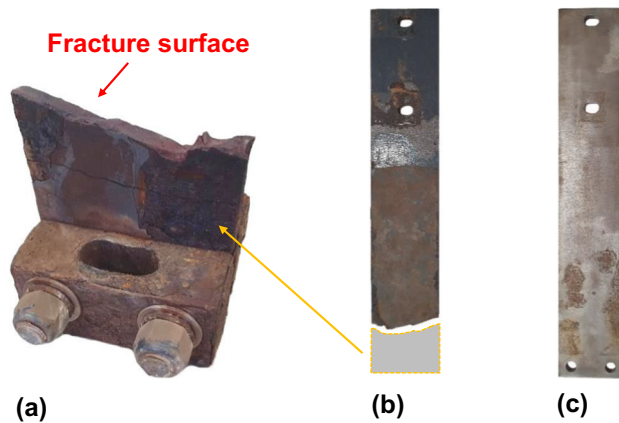
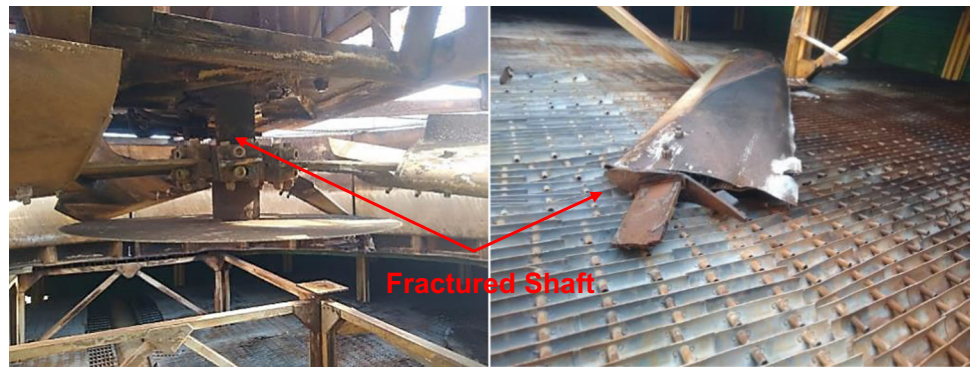


**Fig. 10** Fractured shaft (a) and (b) and intact (c) shaft, as received for analysis



**Fig. 11** The surface of the fracture was analyzed after cleaning

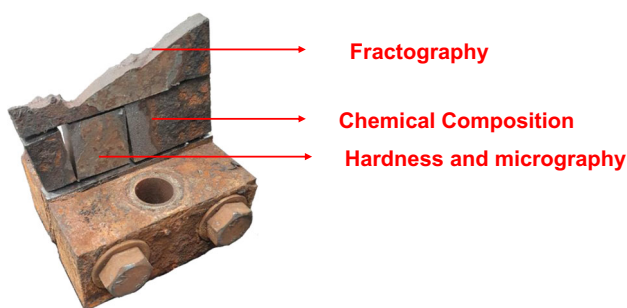


**Fig. 12** The fracture surface analyzed with an emphasis on the sample withdrawal region

chemical compositions for various stainless steels for comparison purposes.

From the results, it can be concluded that the mixer shaft and plate were manufactured from AISI 304L stainless steel (UNS S30403), while the belt was manufactured from AISI 304 steel (UNS S30400).

The mixer paddle, in turn, presented a chemical composition that does not have a direct correspondence with any standard standardized alloy. Most likely, it is an austenitic manganese stainless steel, similar to the AISI 200 family. Here, the contents of Mn (9.15% by weight), Cr (14.06% by weight), and C (0.11% by weight) stand out. At the same time, it was found that this steel was not stabilized.

This type of low-nickel stainless steel (called nickel-saving austenitic stainless steel—NSAs) has been used as an alternative to its more expensive peers (such as the AISI 300 families), in which Ni is substituted by Mn, Cu, C, and N (as austenite stabilizers) in an attempt to reconcile material performance and production cost, as reported by Chu et al. [20].

This material, however, has reduced corrosion resistance (due to the high content of C and not-so-high content of Cr), in addition to a greater susceptibility to intergranular corrosion, mainly when associated with sensitization by processing, as in the case of welding, according to reported in several works, such as those by Chu et al. [20], Quan et al. [21], Song and Guan [22] and Shukla et al. [23].

#### Macrographic Analysis of Component Degradation

Figure 14 illustrates a section cut according to Fig. 7a, where it is possible to observe an advanced state of corrosion in the mixer paddle (the process is concentrated in the paddle and not in the plate) and, more severely, in regions close to the weld (called heat affected zone—HAZ).

It is also possible to note that the plate and the weld do not show corrosion. This is because the highest kinetics of formation of  $\text{Cr}_{23}\text{C}_6$  carbides occurs at temperatures of approximately 450 to 550 °C. This condition was observed for all other upper and lower welds mixer blades (Fig. 15).

**Fig. 13** Planning of miniaturized specimens according to ASTM E8/E8M [18]

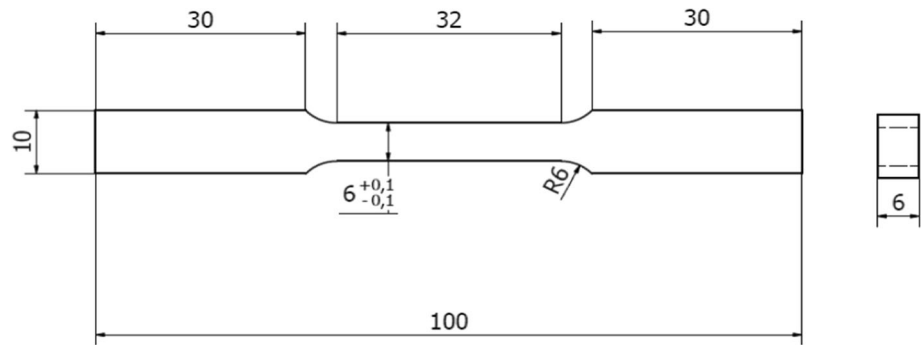


**Table 1** Chemical composition of analyzed samples (%wt.)

Element	C	Mn	Cr	Ni	Mo	Si	P	S	Al	Cu	Nb	Ti	W	V
Axle	0.019	1.866	17.850	7.825	0.398	0.439	0.0353	0.0183	0.003	0.621	0.002	0.003	0.026	0.079
Plate	0.019	1.297	17.427	8.067	0.202	0.358	0.0270	0.0073	0.000	0.254	0.000	0.009	0.011	0.100
Shovel	0.109	9.144	14.067	1.440	0.006	0.500	0.0377	0.0017	0.000	0.390	0.000	0.006	0.011	0.104
Strap	0.053	1.149	17.320	8.152	0.047	0.480	0.0323	0.0017	0.002	0.117	0.000	0.004	0.002	0.047

**Table 2** Chemical composition is standardized according to ASTM A276/A276M [19]

Element	C	Mn	Cr	Ni	Mo	Si	P	S	Al	Cu	Nb	Ti	W	V
304	0.08	2.00	18.0–20.0	8.0–11.0	...	1.00	0.05	0.03	...	...	...	...	...	...
304L	0.03	2.00	18.0–20.0	8.0–12.0	...	1.00	0.05	0.03	...	...	...	...	...	...
201	0.15	5.5–7.5	16.0–18.0	3.5–5.5	...	1.00	0.06	0.03	...	...	...	...	...	...
202	0.15	7.5–10	17.0–19.0	4.0–6.0	...	1.00	0.06	0.03	...	...	...	...	...	...
205	0.12–0.25	14.0–15.5	17.0–19.0	1.0–1.7	...	1.00	0.06	0.03	...	...	...	...	...	...

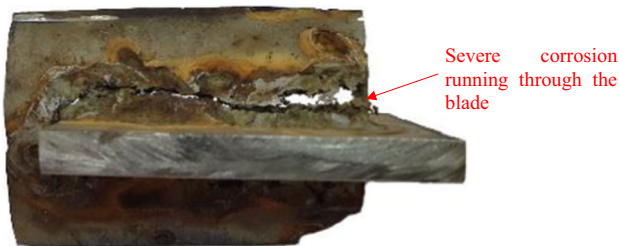


**Fig. 14** Junction point between mixer plate and paddle

The macrograph of the weld bead cross section can be seen in Fig. 9. It is possible to observe severe corrosion starting at the bottom of the blade and advancing toward the interior (point of union with the plate), according to what is shown in Fig. 8. This is indicative that in certain regions close to the weld, the blade was largely sensitized (as will be discussed later).

Figure 16 shows the corrosion of the float straps. Figure 10a shows the specific region where the corrosion manifests itself, which corresponds precisely to the position of the water sheet. Figure 10b shows the details of the corrosive process suffered.

This phenomenon is known as differential aeration corrosion. According to Roberge (2008), the oxygen content of any solution is at the top of the list of factors that influence the corrosion of iron and several other metals. Areas lacking oxygen are anodic, while areas with free access to oxygen are cathodic. Oxygen not only allows for a corrosion reaction by maintaining a cathodic reaction, but it can also promote it. This occurs when there is a difference in dissolved oxygen (DO) concentration between two points on the same metallic surface.

Shaft wear was also analyzed (Fig. 17) close to the attachment point of the mixer plate. As can be seen in Fig. 17b, there are deep marks of abrasive wear. However, as the assembly shows (Fig. 17a), there is no part that, under normal operating conditions, comes into contact with this region since the plain bearing (which has an internal

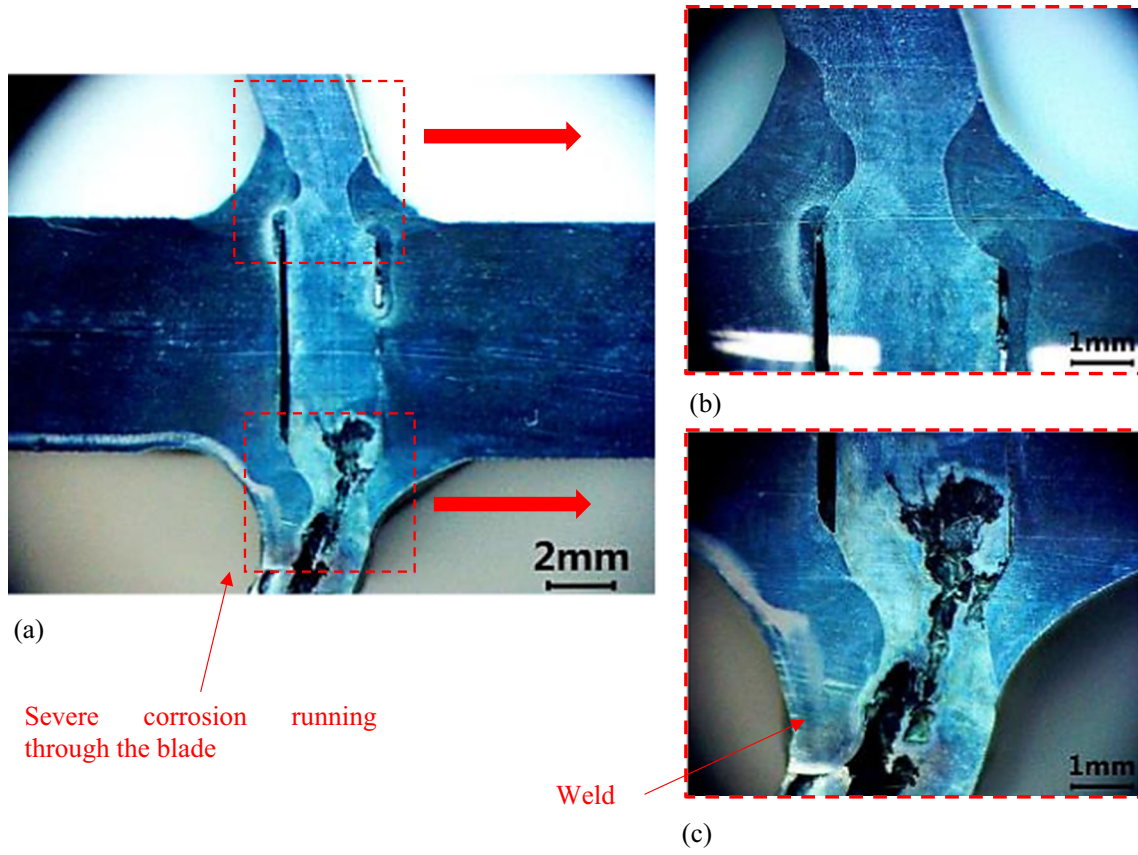


**Fig. 15** Macrograph of the cross section of the union between the paddle and the plate

**Fig. 16** Fastening strap with detail for differential aeration corrosion just below the surface

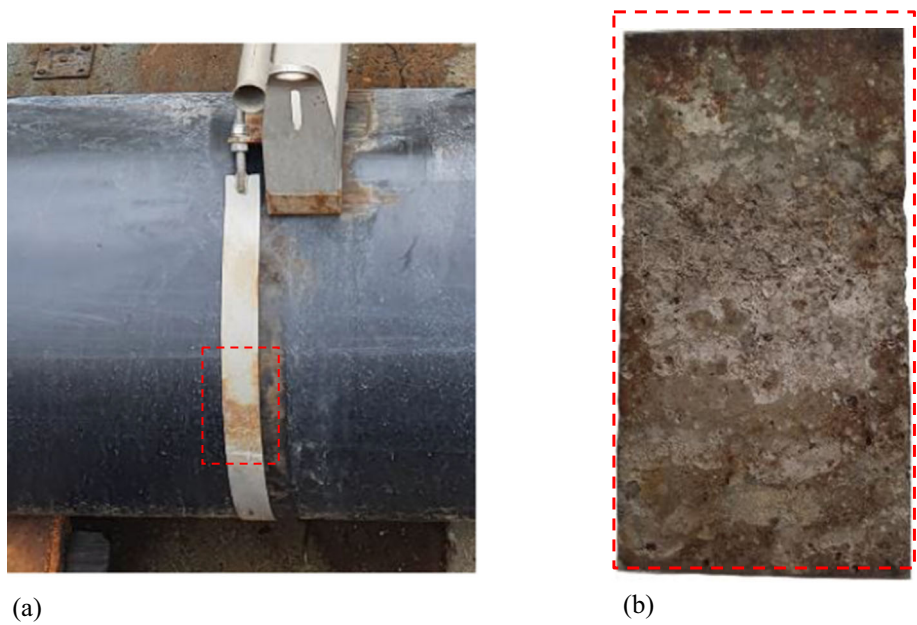
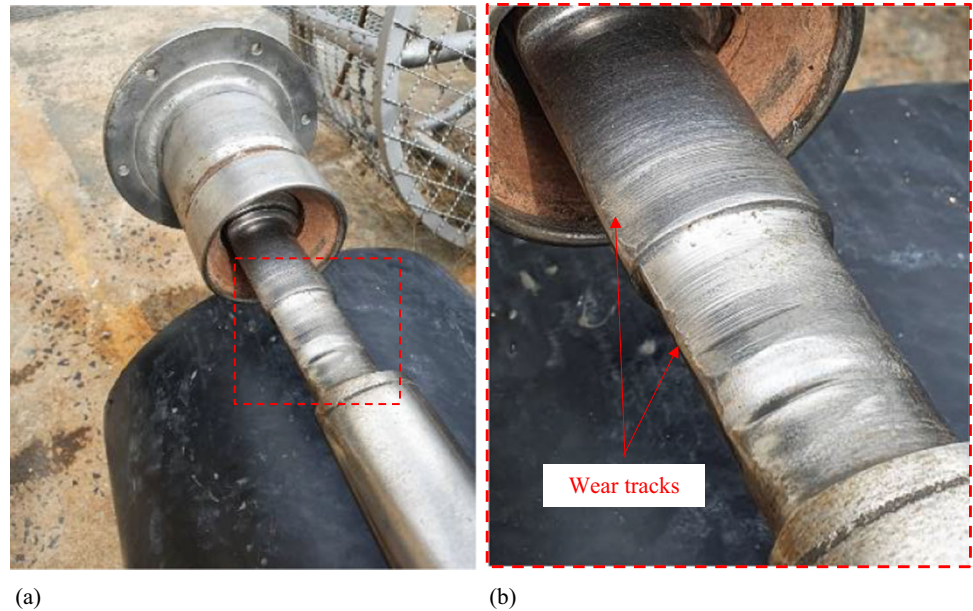




**Fig. 17** Detail of the axle assembly, highlighting the wear suffered



Celeron coating) ends immediately before the point where the diameter reduction begins.

*Macrographic Analysis of Component Degradation*

Figure 18 shows the polished surface of the sample previously shown in Fig. 7b. Analyzes via optical microscopy allowed to observe advanced intergranular corrosion, both in the center of the blade plate (Fig. 18c) and close to the weld (Fig. 18e). In addition to this steel’s susceptibility to intergranular corrosion, the sensitization phenomenon also contributed to the decrease in corrosion resistance observed in Fig. 18d.

According to Dak et al. [24], austenitic stainless steels are subject to precipitation of a constituent at the grain boundary when heated to temperatures between 400 and 900 °C (a phenomenon known as sensitization). This temperature range is commonly reached in the HAZ of welded joints under inadequate cooling conditions (slow cooling).

The most common constituent is Cr<sub>23</sub>C<sub>6</sub> for non-stabilized alloys (without the presence of Nb or Ti), and its formation depletes the regions neighboring the grain boundaries in chromium, which favors intergranular corrosion. According to Song and Guan [22], recommendations to avoid failures caused by sensitization are:

- (a) Reduce the carbon content to values below 0.03% (such as 304L) or add stabilizing elements, such as Ti or Nb.

- (b) Use low heat input and increase solder cooling rates, thus minimizing time in the sensitization temperature range.
- (c) Carry out the post-weld heat treatment, which consists of heating the material to the temperature range of 900–1100 °C to dissolve any carbide in the HAZ.

Figure 13 shows intergranular corrosion, obtained via SEM, where corrosion is observed in regions close to the grain boundaries due to the formation of Cr<sub>23</sub>C<sub>6</sub> carbides at the grain boundaries, leading to a reduction in chromium content in these regions. This makes these regions susceptible to intense corrosion, loss of efficiency, and blade breakage. These failures lead to unbalance in the agitation system and, consequently, high stresses on the shaft bearings, which, in turn, accelerate shaft wear (Fig. 19).

*Hardness*

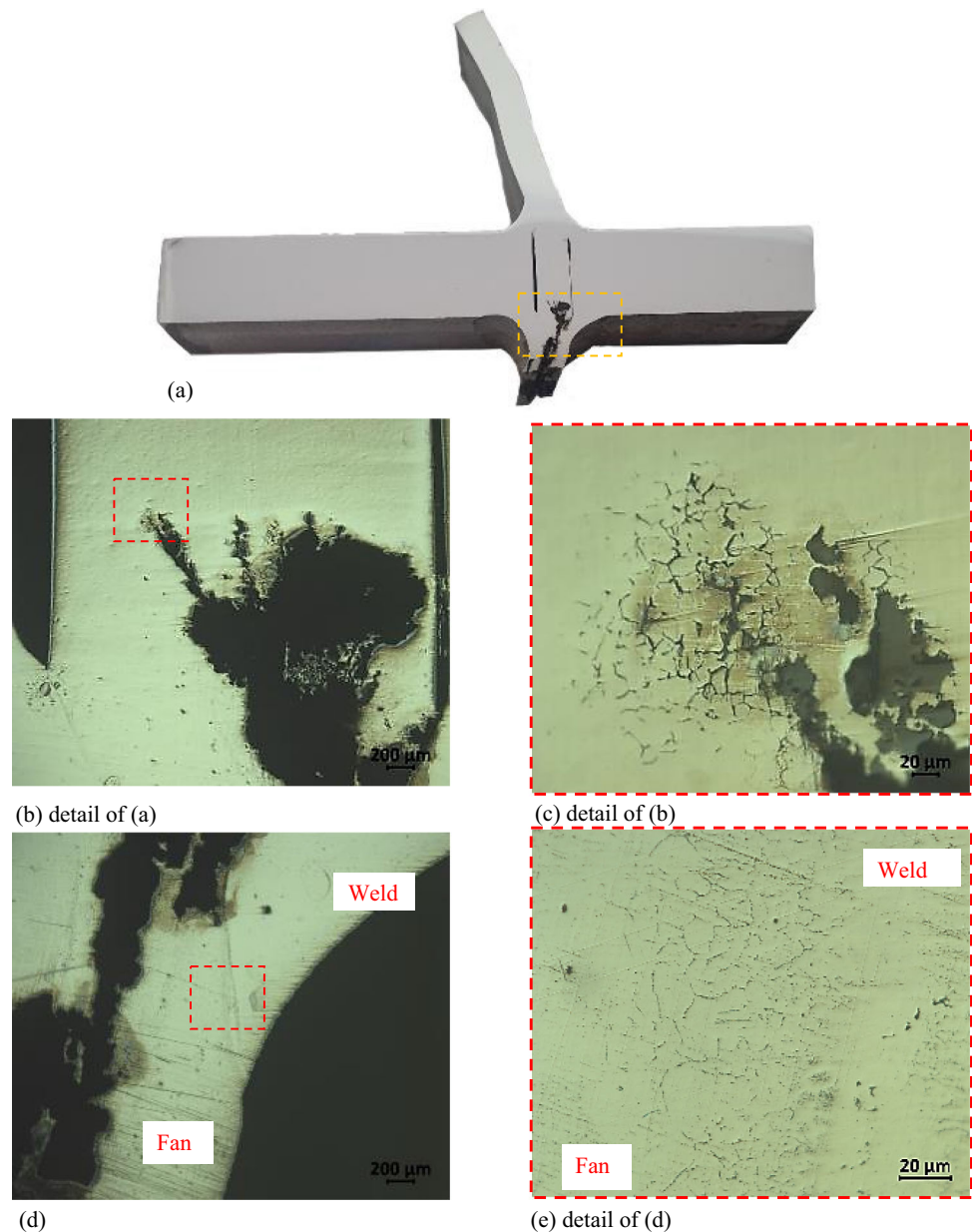
A Vickers hardness measurement was made using the shaft and sample, as shown in Fig. 6. The average of five measurements performed at the center of the axis showed a value of 321.5 ± 6.9 HV1. This hardness value can be attributed to the cold deformation of AISI 304L steel.

*Cooling Tower Fan Blade*

*Chemical Composition*

The chemical compositions of the two rods (“F” for fractured and “I” for intact) can be seen in Table 3. The

**Fig. 18** Micrographs of the bead of the joint between the plate and blade highlight the intergranular corrosion suffered



reference chemical composition (“R”) for the steel STREX 900 from the manufacturer SSAB is also shown.

It is possible to observe that both samples have a remarkably similar chemical composition and are within the ranges specified for the alloy in question, allowing to rule out the chemical composition as a possible cause of fracture.

#### *Chemical Composition*

The results of the tensile tests can be seen in Table 4, with the mean and standard deviation of three tests. The fractured sample had a yield point of  $1049.6 \pm 3.7$  MPa and ultimate tensile strength of  $1079.6 \pm 3.7$  MPa. The intact sample, in turn, presented a yield point of  $1002.6 \pm 7.0$  MPa, and a strength limit of  $1042.3 \pm 8.2$  MPa. The values were within the expected, considering the reference values informed by the manufacturer.

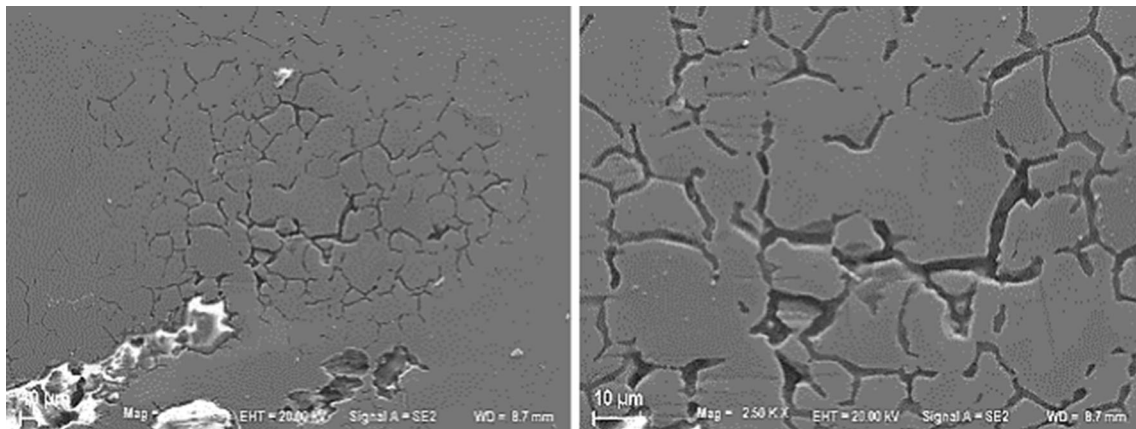


**Fig. 19** Scanning electron microscopy images of intergranular corrosion on the mixer paddle (manganese austenitic stainless steel)

**Table 3** Chemical composition of the analyzed samples, “R” being the reference composition, “F” the fractured sample, and “I” the intact sample (% by weight)

	C	Mn	Si	P	S	Cr	Ni	Mo	Al	Cu	Ti	W	V	Nb	B
R	0.20 max	1.60 max	0.50 max	0.02 max	0.01 max	0.80 max	2.00 max	0.70 max	...	0.30 max	...	...	...	...	0.005 max
F	0.188	1.053	0.258	0.015	0.001	0.579	0.05	0.571	0.1	0.039	0.005	0	0	0.022	0.003
I	0.186	1.11	0.299	0.011	0	0.612	0.047	0.552	0.1	0.017	0.005	0	0	0.026	0.003

**Table 4** Tensile test results, with the mean and standard deviation

Sample	Yield strength-MPa	Ultimate tensile strength-MPa
Reference	900	940 to 1100
Fractured	1049.6 ± 3.7	1079.6 ± 3.7
Intact	1002.6 ± 7.0	1042.3 ± 8.2

**Hardness**

For hardness analysis, samples were taken from both rods, and measurements were taken along the cross section (12.7 mm). Eight points were measured per sample, with a spacing of 1.5 mm between each indentation. The results are graphically shown in Fig. 20.

The intact sample presented an average hardness of 358 ± 7 HV1, while the fractured sample presented a value of 376 ± 12 HV1. These are the values commonly found for high-strength, low-alloy (HRBL) steels that have been quenched and tempered (as shown in the Micrographs section). No hardness gradient was found along with the thickness or significant difference between the samples, which could justify the fracture.

**Micrography**

The microstructures found can be seen in Fig. 21 for the fractured sample and Fig. 22 for the intact sample. It is possible to observe a quenched and tempered martensitic microstructure in both samples, with no variation in the components’ thickness. No evidence of nonconformity in relation to the microstructure that could cause component fracture was found.

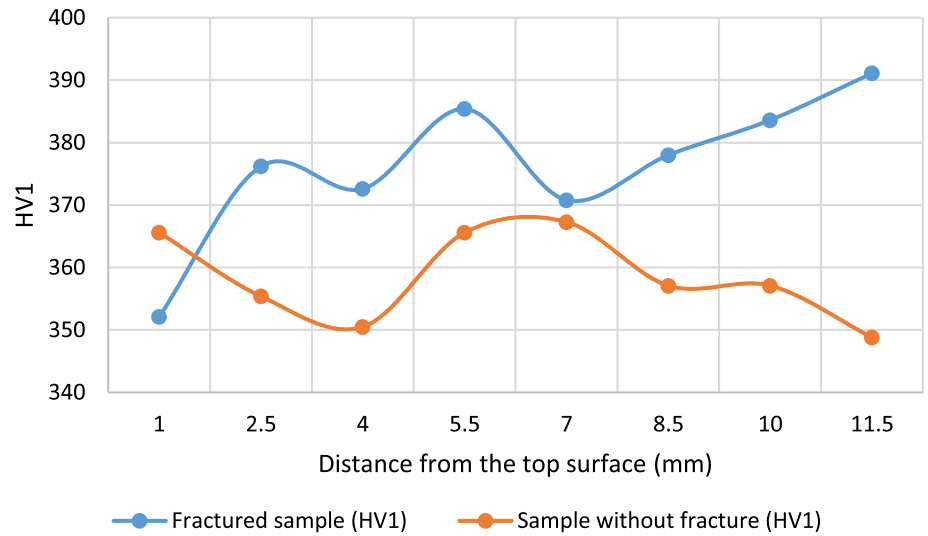
**Fractography**

The fracture surface can be seen in Fig. 23. Figure 23a shows the surface divided into regions of interest. White lines demonstrate the fatigue crack propagation fronts in each region.

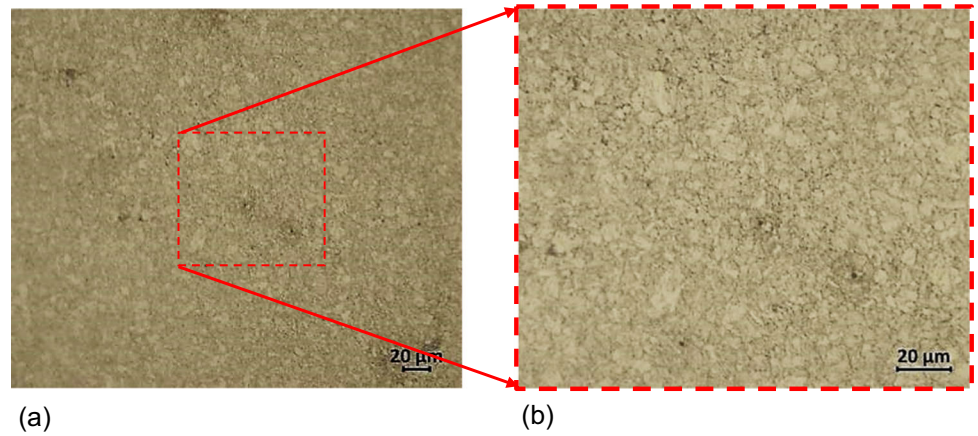
Figure 23b shows a fracture region during the part rupture’s last stage and some fatigue cracks that started (yellow arrows) on the surface of maximum tensile stress. Figure 23c shows region 2, where it is also possible to observe crack propagation (white line in Fig. 23a).

Figure 23d, in turn, shows a smooth-looking region characteristic of fatigue fracture. The crack nucleated in the upper part of the rod (in the figure, it corresponds to the lower part), which was subjected to cyclic tensile stresses (due to its weight) and the drag force due to the upward flow of air). Comparing the areas of fatigue crack

**Fig. 20** Hardness values were found for both rods in HV1



**Fig. 21** Micrographs of the microstructure of the fractured sample revealed with 2% Nital



**Fig. 22** Micrographs of the intact sample microstructure were developed with 2% Nital

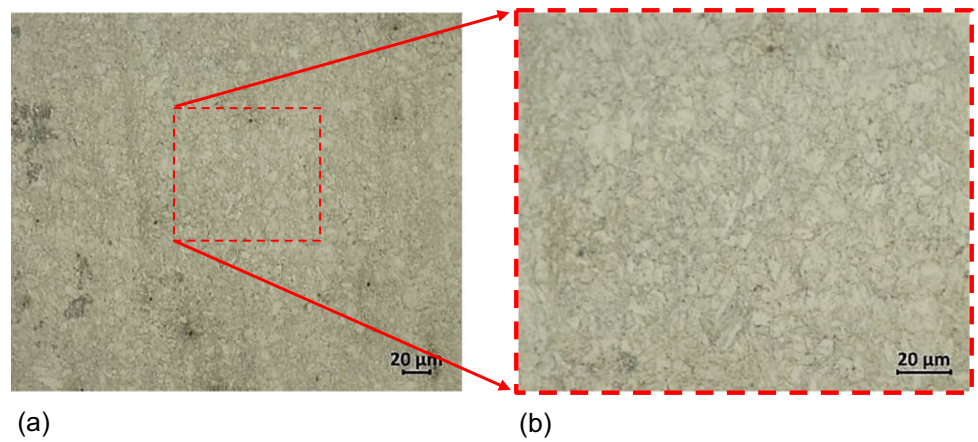
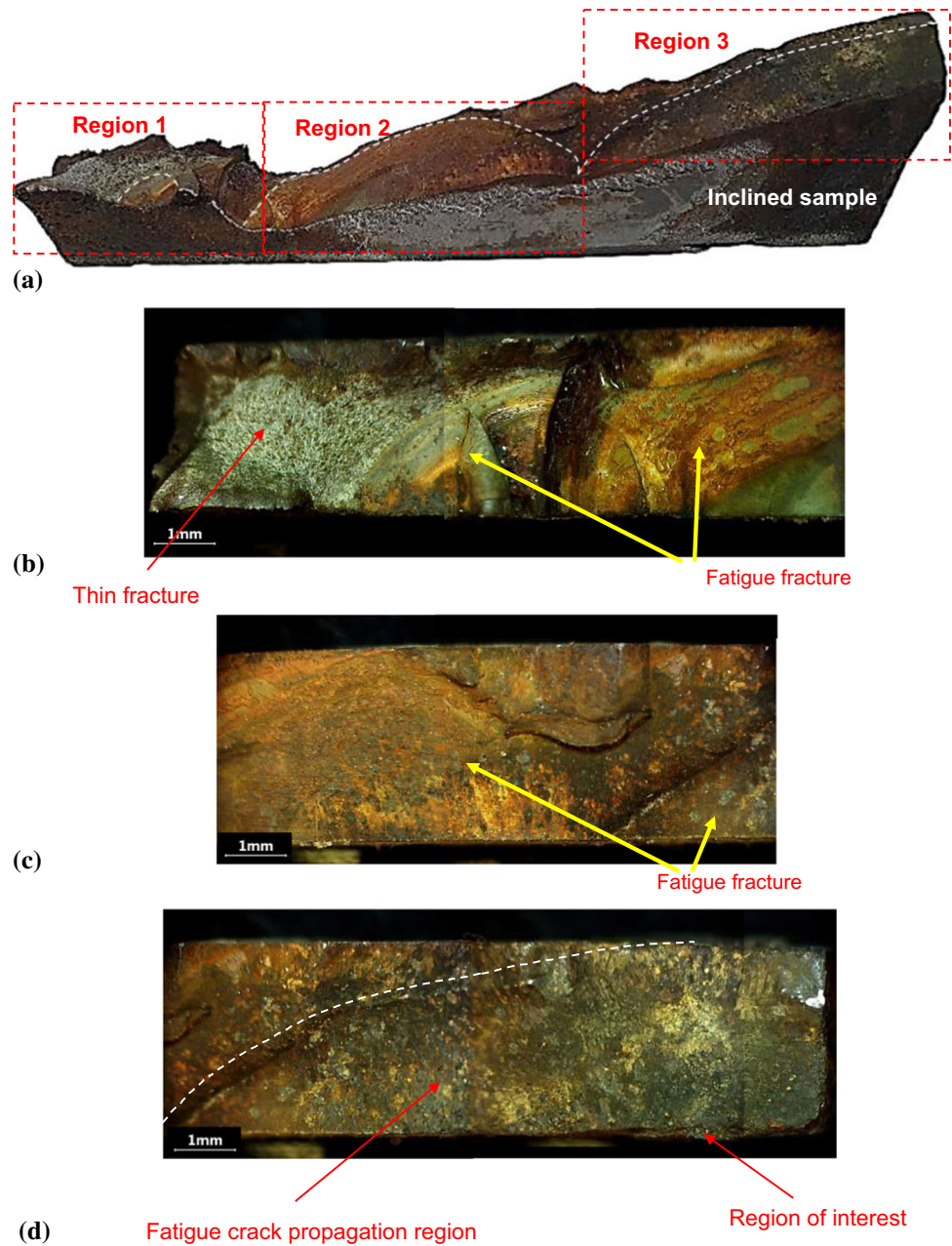


**Fig. 23** Macrographs of the fracture region were observed using stereomicroscopy. (a) fracture region with emphasis on regions of interest for failure analysis; (b) macrographs of region 1; (c) macrographs of region 2; (d) macrographs of region 3



propagation and the area corresponding to the final fracture, it can be concluded that the loads were of low amplitude.

Figure 24 shows the fracture region, highlighting the region of interest 3. Figure 24c and d shows the edge inclined at 45° to show the corrosion pits.

As shown in Fig. 24, several corrosion pits have formed on the top of the stem. These corrosion pits probably functioned as nucleation points for one or more cracks, which evolved to abrupt rupture since the cross section was reduced so that it did not support the loads involved in the component’s operation.

In order to confirm the hypothesis of cracks being formed from points of localized corrosion (which functioned as points of stress concentration), samples were taken from both rods, as shown in Fig. 25. Each sample was approximately 40 mm in thickness and length, having been analyzed in the longitudinal section of the stem.

As can be seen in Fig. 26, cracks at the beginning of propagation were found in at least three different points of the fractured nail, with lengths between 0.3 and 0.65 mm. All cracks observed started from corrosion points.

No cracks of the same type or size were found for the intact stem, but images obtained via SEM (Fig. 27) showed several points of localized corrosion. It is important to note

**Fig. 24** Macrographs of the region of interest 2 (see Fig. 10d) showing the cross section (a and b) and the 45° angled edge (c and d)

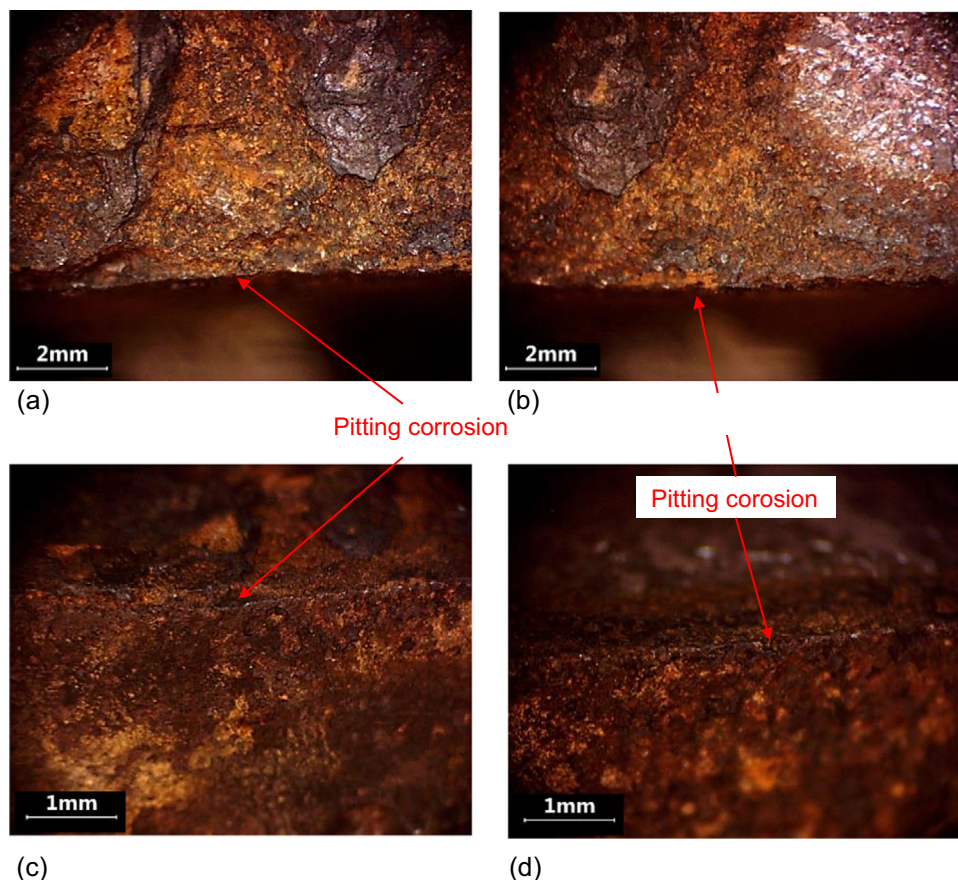


**Fig. 25** Place of removal of samples to search for cracks

that before being sent for analysis, the intact stem was blasted to remove corrosion products and paint and this process may have masked surface effects such as those observed for the fractured stem.

Figure 27a and b shows corrosion pits of the same type found via light microscopy for the fractured stem (Figs. 25 and 26). Figure 27c and d shows surface defects (from corrosion or porosity of the material) that could evolve into cracks and eventually generate the same type of failure presented by the fractured stem.

Another hypothesis for the present behavior, that is, one nail fails, and the others do not, is that the fractured nail worked under fluctuating loads different from those experienced by the other nails.

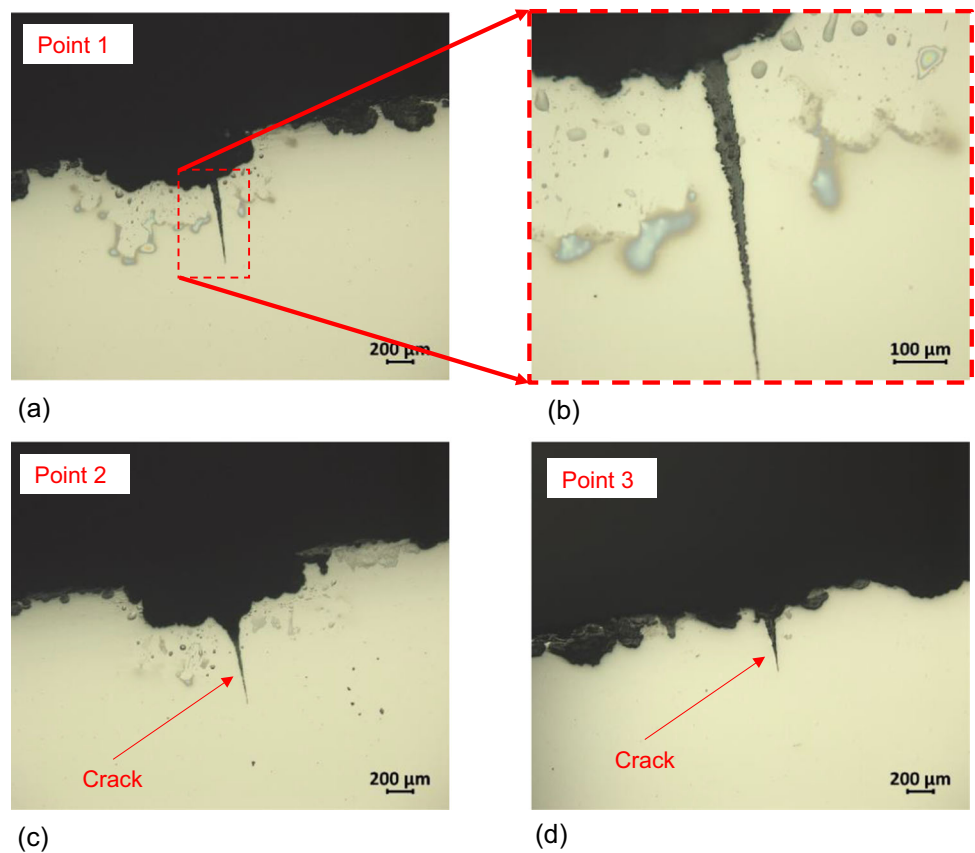
## Conclusions

Through the present investigation, macro and micrographic investigations, hardness measurements, and chemical composition analyses of several components of an aerator/mixer and a cooling tower fan blade.

Regarding the aerator/mixer used to treat industrial effluents, the results obtained allow us to conclude that:

- The mixer shaft and plate were made of AISI 304L stainless steel. No signs of corrosion were found in these materials, which ensures the suitability of this alloy for the processes used to manufacture the equipment (welding) and the environment where it is used;
- The float fastening strap was made of AISI 304 steel. Due to differential aeration corrosion, it is suggested that steel with greater corrosion resistance, such as AISI 316, be used;
- The mixer paddle was made of manganese austenitic stainless steel, whose susceptibility to intergranular corrosion was increased due to the sensitization phenomenon during welding on the plate. It is recommended that, for its manufacture, the same material as the plate (AISI 304L) is used, and the

**Fig. 26** Micrographs of the cross section of the fractured nail highlighting the cracks observed



welding process is carried out with the appropriate procedures to avoid sensitization;

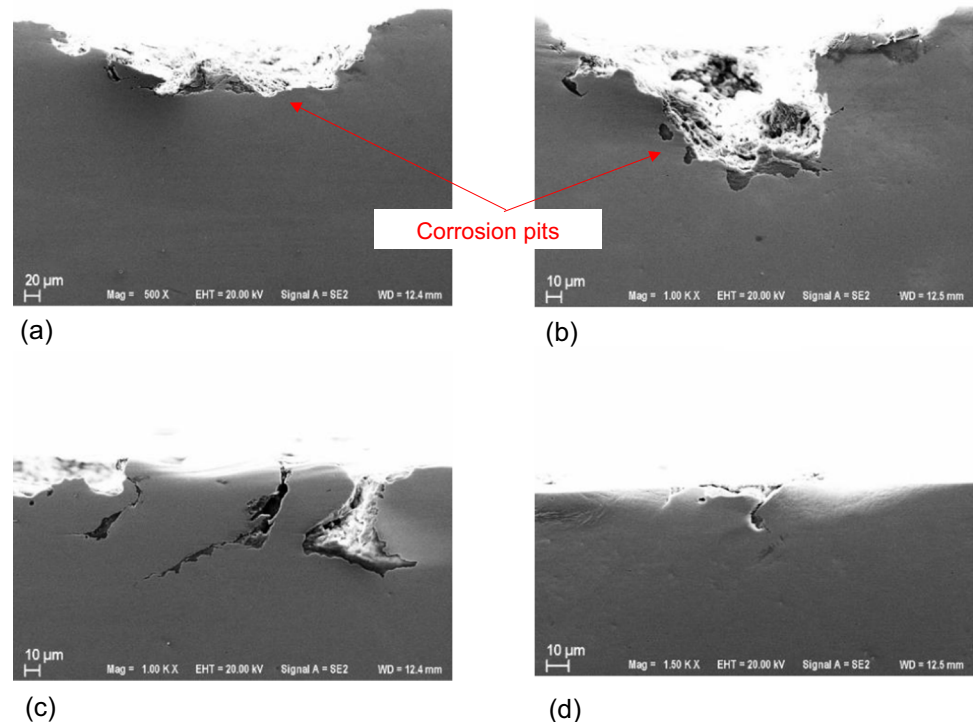
- The problems presented in the shaft (ovalization and reduction of diameter) occurred due to the unbalance of the plate, which, in turn, was caused by the breakage/corrosion of the blades. This corrosion was due to the inadequacy of the blades' steel for the environment in which they are used.
- For the above, it is recommended that the failure of the protective coating against corrosion be avoided, thus avoiding the formation of pits that can act as stress concentration points and, thus, regions of facilitated nucleation of cracks.

Regarding the cooling tower fan blade, the results obtained allow us to conclude that:

- The chemical composition of both rods is compatible with the material specified in the project (STRENX 900);

- Tensile tests indicated that the yield strength of the fractured stem is  $1079.6 \pm 3.7$  MPa and that of the intact stem is  $1002.6 \pm 7.0$  MPa, which is compatible with the strength of the reference;
- Hardness measurements showed that there is no hardness gradient across the thickness. The values found are compatible with those expected for tempered ARBL steel;
- Metallographic analyzes showed that both rods have a martensitic microstructure, tempered and quite refined, without microstructural variations along with the thickness or width of the pieces;
- Based on fractography, it is possible to state that the failure occurred due to fatigue under low-amplitude loads that caused the nucleation of cracks facilitated due to the presence of corrosion pits in the upper part of the stem;
- For the above, it is recommended to avoid the failure of the protective coating against corrosion, thus avoiding

**Fig. 27** Electron microscopy of the intact stem, highlighting the effects of surface corrosion and surface defects



the formation of pits that can act as stress concentration points and, thus, regions of facilitated nucleation of cracks.

## References

1. A. Heng, S. Zhang, A.C.C. Tan, J. Mathew, Rotating machinery prognostics: state of the art, challenges and opportunities. *Mech. Syst. Signal Process.* **23**, 724–739 (2009). <https://doi.org/10.1016/j.ymssp.2008.06.009>
2. V.N. Chuvil'deev, V.I. Kopylov, N.N. Berendeev, A.A. Mura-shov, A.V. Nokhrin, M.Y. Gryaznov, I.S. Shadrina, N.Y. Tabachkova, C.V. Likhmitskii, D.N. Kotkov, P.V. Tryaev, Corrosion fatigue crack initiation in ultrafine-grained near- $\alpha$  titanium alloy PT7M prepared by rotary swaging. *J. Alloys Compd.* **790**, 347–362 (2019). <https://doi.org/10.1016/j.jallcom.2019.03.146>
3. R. Ebara, Corrosion fatigue phenomena learned from failure analysis. *Eng. Fail. Anal.* **13**, 516–525 (2006). <https://doi.org/10.1016/j.engfailanal.2004.12.024>
4. O. Adedipe, F. Brennan, A. Kolios, Review of corrosion fatigue in offshore structures: present status and challenges in the offshore wind sector. *Renew. Sustain. Energy Rev.* **61**, 141–154 (2016). <https://doi.org/10.1016/j.rser.2016.02.017>
5. C.D. Lundin, Dissimilar Metal Welds-Transition Joints Literature Review Emphasis is on carbon migration, the stress/strain state of welds, and transition joint failure mechanisms (1982)
6. C.R. Corleto, G.R. Argade, Failure analysis of dissimilar weld in heat exchanger. *Case Stud. Eng. Fail. Anal.* **9**, 27–34 (2017). <https://doi.org/10.1016/j.csefa.2017.05.003>
7. M. Alizadeh-Sh, S.P.H. Marashi, Resistance spot welding of dissimilar austenitic/duplex stainless steels: microstructural evolution and failure mode analysis. *J. Manuf. Process.* **28**, 186–196 (2017). <https://doi.org/10.1016/j.jmapro.2017.06.005>
8. J. Verma, R.V. Taiwade, Dissimilar welding behavior of 22% Cr series stainless steel with 316L and its corrosion resistance in modified aggressive environment. *J. Manuf. Process.* **24**, 1–10 (2016). <https://doi.org/10.1016/j.jmapro.2016.07.001>
9. N. Udoye, O.S.I. Fayomi, A. Inegbenebor, Review on performance of existing cooling tower fan blade in the production industry, *International Journal of Mechanical. Eng. Technol.* **10**, 1833–1839 (2019)
10. B. Padasale, J.K.R. Kumar, P.R. Sondar, S. Govindarajan, S.R. Hegde, Failure analysis of cooling tower fan-arm. *J. Fail. Anal. Prev.* **20**, 1417–1425 (2020). <https://doi.org/10.1007/s11668-020-00947-1>
11. H. Kazempour-Liacy, M. Mehdizadeh, M. Akbari-Garakani, S. Abouali, Corrosion and fatigue failure analysis of a forced draft fan blade. *Eng. Fail. Anal.* **18**, 1193–1202 (2011). <https://doi.org/10.1016/j.engfailanal.2011.02.014>
12. S.R. Hegde, J.K. Rakshan Kumar, P. Sondar, P.C. Dsilva, Catastrophic failure of urea prill-tower fan. *Eng. Fail. Anal.* (2021). <https://doi.org/10.1016/j.engfailanal.2020.105207>
13. C. Medrea, D.G. Papageorgiou, H. Bravos, I. Chicinaş, Failure analysis of a fan blade holding assemblage, installed on the cooling tower of a power plant. *Eng. Fail. Anal.* (2021). <https://doi.org/10.1016/j.engfailanal.2021.105505>
14. ASTM E3-11, Standard guide for preparation of metallographic specimens 1, American Society for Testing and Materials. (2017). <https://doi.org/10.1520/E0003-11>
15. ASTM E407-07, Standard practice for microetching metals and alloys, American Society for Testing and Materials. (2016). <https://www.astm.org/e0407-07r15e01.html>. Accessed 5 July 2022
16. ASTM E92-17, Standard test methods for Vickers hardness and Knoop hardness of metallic materials, American Society for



- Testing and Materials. (2016). <https://www.astm.org/e0092-17.html>. Accessed 5 July 2022.
17. ASTM E140-12B, Standard hardness conversion tables for metals relationship among Brinell hardness, Vickers hardness, Rockwell hardness, superficial hardness, Knoop hardness, Scleroscope hardness, and Leeb hardness, American Society for Testing and Materials. (2019). <https://www.astm.org/e0140-12br19e01.html>. Accessed 5 July 2022.
  18. ASTM E8-04, American Society for Testing and Materials, American Society for Testing and Materials. (2010).
  19. ASTM A276/A276M-17, Standard Specification for Stainless Steel Bars and Shapes, American Society for Testing and Materials. (2017).
  20. K.H. Chu, C.C. Lam, Y.F. Sun, V.A.M. Cristino, C.T. Kwok, H. Pan, K.H. Lo, Chloride stress corrosion cracking of a non-standard, ‘Borderline’ Chromium-Manganese stainless steel—problems of counterfeits and substandard materials. *Eng. Fail. Anal.* **127**, 105562 (2021). <https://doi.org/10.1016/j.engfailanal.2021.105562>
  21. S. Quan, L. Wang, R. Song, Y. Wang, T. Wang, Y. Su, Effects of sensitization induced intercrystalline precipitation on mechanical properties of 204C2 nickel-saving austenitic stainless steel. *Vacuum*. **183**, 109805 (2021). <https://doi.org/10.1016/j.vacuum.2020.109805>
  22. M. Song, K. Guan, Failure analysis of a weld-decayed austenitic stainless steel. *Eng. Fail. Anal.* **18**, 1613–1618 (2011). <https://doi.org/10.1016/j.engfailanal.2011.05.019>
  23. S. Shukla, A.P. Patil, A.P. Kawale, R.K. Haldkar, A. Dahiwal, A. Bansod, Effect of grain refinement on sensitization of high manganese austenitic stainless steel. *Mater. Today Proc.* **44**, 2802–2807 (2021). <https://doi.org/10.1016/j.matpr.2020.12.833>
  24. G. Dak, C. Pandey, A critical review on dissimilar welds joint between martensitic and austenitic steel for power plant application. *J. Manuf. Process.* **58**, 377–406 (2020). <https://doi.org/10.1016/j.jmapro.2020.08.019>
- Publisher’s Note** Springer Nature remains neutral with regard to jurisdictional claims in published maps and institutional affiliations.
- Springer Nature or its licensor (e.g. a society or other partner) holds exclusive rights to this article under a publishing agreement with the author(s) or other rightsholder(s); author self-archiving of the accepted manuscript version of this article is solely governed by the terms of such publishing agreement and applicable law.